

# Regulating the Local Reaction Microenvironment at Chromium Metal–Organic Frameworks for Efficient H<sub>2</sub>O<sub>2</sub> Electrosynthesis in Neutral Electrolytes

Zhihao Pei, Yan Guo, Deyan Luan, Xiaojun Gu,\* and Xiong Wen (David) Lou\*

The electrochemical synthesis of hydrogen peroxide represents a promising alternative to the traditional anthraquinone process, aiming for zero pollution. However, achieving efficient electrochemical synthesis of hydrogen peroxide in neutral electrolytes is challenging due to the sluggish kinetics of the two-electron oxygen reduction reaction. To address this issue, a unique metal–organic framework (MOF) featuring Cr metal sites coordinated with tetrabromoterephthalic acid (Cr-TBA) is synthesized. This specially designed MOF exhibits a distinctive paper-clip-like structure and remarkably enhanced Lewis acidity. Experimental results demonstrate that the obtained structure can facilitate the attraction of OH<sup>−</sup> ions in solution, promoting their accumulation on the catalyst surface. This enhancement leads to excellent performances of Cr-TBA in neutral electrolytes, achieving Faradaic efficiencies of 96–98% and a production rate of 13.4 mol g<sub>cat</sub><sup>−1</sup> h<sup>−1</sup> at the current density of 150 mA cm<sup>−2</sup>. Operando spectroscopy and density functional theory calculations indicate that this modified microenvironment effectively facilitates the conversion of the <sup>•</sup>OOH intermediates to H<sub>2</sub>O<sub>2</sub> on the catalyst surface.

H<sub>2</sub>O<sub>2</sub> production, capitalizing on its inherent safety, simplified operational protocols, and environmentally friendly nature.<sup>[3,4]</sup> This approach leverages renewable energy sources, thus deviating from conventional methodologies. Recently, the electrochemical two-electron oxygen reduction reaction (2e<sup>−</sup> ORR) has gained considerable attention as a highly promising pathway for H<sub>2</sub>O<sub>2</sub> synthesis.<sup>[5]</sup> However, this reaction competes with the four-electron ORR, leading to the undesired formation of H<sub>2</sub>O.<sup>[6]</sup> Consequently, extensive research endeavors currently focus on developing tailored electrocatalysts to achieve a selective reduction of O<sub>2</sub> to H<sub>2</sub>O<sub>2</sub>.

Technologically, the 2e<sup>−</sup> ORR can be conducted over a wide pH range, spanning from 0 to 14.<sup>[7]</sup> Among these, the electrocatalytic synthesis of H<sub>2</sub>O<sub>2</sub> under alkaline conditions has been extensively investigated with satisfactory performances.<sup>[8–11]</sup> Additionally, numerous studies aim to produce

## 1. Introduction

Hydrogen peroxide (H<sub>2</sub>O<sub>2</sub>) possesses versatile oxidizing properties and holds substantial potential as an energy carrier, making it highly valuable across diverse scientific domains.<sup>[1]</sup> Currently, the industrial-scale synthesis of H<sub>2</sub>O<sub>2</sub> predominantly relies on the anthraquinone process, which necessitates extensive infrastructure, intricate operational procedures, high costs associated with storage and transportation, and generates considerable waste and pollution.<sup>[2]</sup> In contrast, the electrochemical route has emerged as a promising alternative for on-site

acidic H<sub>2</sub>O<sub>2</sub> solution for oxidizing purposes in wastewater treatment, organic degradation, and chemical upgrading as well.<sup>[12–15]</sup> In contrast to the extensive research of electrochemical synthesis of H<sub>2</sub>O<sub>2</sub> under alkaline and acid conditions, less effort has been devoted to the 2e<sup>−</sup> ORR research in neutral media.<sup>[16]</sup> This is primarily due to the low concentrations of H<sup>+</sup> and OH<sup>−</sup> ions in neutral environments, which hinders the ORR kinetics.<sup>[17,18]</sup> Nevertheless, neutral H<sub>2</sub>O<sub>2</sub> solutions are more commonly used in practical applications, such as household cleaning and gardening, due to their versatility and the added advantage of avoiding secondary costs associated with neutralizing acidic or alkaline solutions.<sup>[7]</sup> Furthermore, the utilization of neutral electrolytes for electrochemical synthesis of H<sub>2</sub>O<sub>2</sub> offers the advantage of reducing equipment and material losses and minimizing corrosion costs during long-term operation.<sup>[19]</sup> Therefore, there is a pressing need to address the challenges associated with low reaction efficiency and yield in neutral electrolytes and to advance the development of electrocatalysts for electrochemical synthesis of H<sub>2</sub>O<sub>2</sub> in neutral media. This necessitates the design of efficient electrocatalysts through the exploration of novel mechanisms or the development of effective regulation strategies with dedicated efforts.

As we know, the catalytic performance is greatly influenced by the local chemical environment around the catalyst.<sup>[20,21]</sup>

Z. Pei, D. Luan, X. W. Lou  
Department of Chemistry  
City University of Hong Kong  
83 Tat Chee Avenue, Kowloon, Hong Kong 999077, China  
E-mail: david.lou@cityu.edu.hk

Y. Guo, X. Gu  
School of Chemistry and Chemical Engineering  
Inner Mongolia University  
Hohhot 010021, China  
E-mail: xiaojun.gu@imu.edu.cn

The ORCID identification number(s) for the author(s) of this article can be found under <https://doi.org/10.1002/adma.202500274>

DOI: 10.1002/adma.202500274

Theoretically, in neutral electrolytes, the production of  $\text{OH}^-$  during the electrochemical synthesis of  $\text{H}_2\text{O}_2$  process can increase the local pH at the catalytic sites, thus facilitating the mass transfer. However, for conventional catalysts, the  $\text{OH}^-$  ions often diffuse quickly into the bulk electrolyte, driven by the concentration gradient, which slows the increase in local pH and catalytic performance. Therefore, effectively confining  $\text{OH}^-$  near the catalytic sites to boost local pH is a crucial yet challenging task, especially for the electrochemical synthesis of  $\text{H}_2\text{O}_2$  process.

Herein, a metal–organic framework (MOF) constructed by Cr metal sites coordinated with a tetrabromoterephthalic acid (TBA) ligand (denoted as Cr-TBA) is developed via an elaborately designed crystal nucleation and growth process. N-methylacridone (NMA) fluorescence results indicate that the introduction of TBA ligand leads to a noticeable increase in the Lewis acidity of the catalysts. This enhancement promotes the local accumulation of  $\text{OH}^-$  ions around the catalyst surface during the electrochemical synthesis of  $\text{H}_2\text{O}_2$  process. Furthermore, operando spectroscopy and density functional theory (DFT) calculations substantiate the modification of the local microenvironment has a positive impact on the formation of  $\text{H}_2\text{O}_2$  from  $\text{OOH}^*$  intermediates. The above regulation strategy facilitates the performances of electrochemical synthesis of  $\text{H}_2\text{O}_2$  in a neutral medium, achieving remarkable Faradaic efficiencies of 96% to 98% at current densities ranging from 50 to 150  $\text{mA cm}^{-2}$ . Additionally, the optimized microenvironment enables Cr-TBA to reach a maximum  $\text{H}_2\text{O}_2$  production rate of 13.4  $\text{mol g}_{\text{cat}}^{-1} \text{h}^{-1}$ . Consequently, the Cr-TBA catalyst emerges as one of the most promising electrocatalysts for  $2\text{e}^-$  ORR.

## 2. Results and Discussion

A MOF constructed by Cr metal sites coordinated with terephthalic acid (MIL-101 (Cr)) is synthesized according to the previous literature with some modifications (Figure S1, Supporting Information).<sup>[22]</sup> The resulting MIL-101 (Cr) exhibits substantially enhanced performance for electrochemical synthesis of  $\text{H}_2\text{O}_2$  under alkaline conditions (0.1 M KOH, pH 13) compared to neutral conditions (0.1 M  $\text{K}_2\text{SO}_4$ , pH 7.4) (Figures S2 and S3, Supporting Information). This observation prompts us to explore the creation of a favorable alkalized local reaction environment to improve the kinetics and efficiency of  $\text{H}_2\text{O}_2$  electrosynthesis. The hard and soft acid base theory suggests that a hard acid preferentially interacts with a hard base.<sup>[23]</sup> Guided by the above principle, we propose that the alkalized microenvironment could be artificially created by introducing the Lewis acid or increasing the Lewis acidity of the materials. Since hydroxyl anions are hard Lewis bases, these modified materials could facilitate to capture of them from the solution. To test this hypothesis, the strong electron-withdrawing groups are introduced onto the terephthalic acid ligand. This modification could enhance the Lewis acidity of the material and allow for precise regulation of the microenvironment during the reaction process, as verified in the following experimental section.

**Figure 1a** illustrates the synthetic schematic of Cr-TBA. The unique paper-clip structured Cr-TBA, with an average length of  $\approx 5.0 \mu\text{m}$ , is synthesized via a solvothermal reaction followed by the removal of cetrimonium bromide (CTAB). To clarify the structure formation mechanism and the role of CTAB, Cr-TBA sam-

ples with and without CTAB at varied reaction times are synthesized. As illustrated in Figure S4a–c (Supporting Information), the CTAB-free samples exhibit the following morphology evolution process. At 250 min reaction time, some obvious large particles can be observed. Subsequently, a prolonged reaction (500 min) leads to the complete transformation into small particles. Upon arriving 1000 min, nanoparticle aggregation becomes evident. In the case of the CTAB-containing samples, at the initial stage (60 min reaction), coexisting particles and localized paper-clip-like structures can be observed (Figure S4d, Supporting Information). Then, continued reaction promotes directional growth of paper-clip structures, accompanied by particle refinement (Figure S4e, Supporting Information). After 1000 min reaction, the unique paper-clip-like structure composed of small nanoparticles is fully developed (Figure S4f, Supporting Information). The comparative analysis with Figure S4a–c (Supporting Information) reveals that the particle refinement occurs independent of CTAB, driven primarily by the solvothermal condition. In addition, unlike the CTAB-free sample, the structural evolution of the CTAB-containing samples shows CTAB-dependent anisotropic growth rather than isotropic aggregation, thus exclusively inducing the formation of the paper-clip-like structure. Specifically, during the reaction, large particles begin to dissolve under high temperature and pressure conditions. At this stage, the high surface energy of the formed MOF nanocrystals causes CTAB molecules to rapidly and strongly adsorb onto their surfaces. In this context, CTAB could act as both a stabilizer and a dispersant, kinetically controlling the morphology of the nanocrystals through selective adsorption and desorption, thereby promoting the formation of the thermodynamically stable paper-clip-like structure.<sup>[24,25]</sup> In addition, the impact of CTAB concentrations on the morphology of Cr-TBA is explored via the synthesis with different concentrations of CTAB labeled as: Cr-TBA-0 (no CTAB added), Cr-TBA-1 (CTAB concentration of 1  $\text{mg mL}^{-1}$ ), Cr-TBA (CTAB concentration of 2.5  $\text{mg mL}^{-1}$ , which is the main sample discussed in this work), and Cr-TBA-3.5 (CTAB concentration of 3.5  $\text{mg mL}^{-1}$ ). The Cr-TBA-0 sample exhibits an irregular morphology characterized by particle stacking. As expected, the addition of CTAB will greatly influence the morphology of formed products. At a CTAB concentration of 2.5  $\text{mg mL}^{-1}$ , the material exhibits a paper-clip shape structure. However, further increasing the CTAB concentration slightly compromises the crystallinity and morphology (Figures S5 and S6, Supporting Information). Moreover, the slightly modified strategy has also been applied to the synthesis of a MOF constructed by Cr metal sites coordinated with the 2-nitroterephthalic acid ligand (MIL-101- $\text{NO}_2$  (Cr)) via a similar approach (Figure S7, Supporting Information).

The field-emission scanning electron microscopy (FESEM) and transmission electron microscopy (TEM) images show well-formed paper-clip-like structures (Figure 1b,c). Meanwhile, some lattice fringes with a lattice spacing of  $\approx 0.35 \text{ nm}$  could be observed, matching the  $d$ -spacing of the most obvious diffraction peak at  $\approx 2\theta = 25.5^\circ$  (Figures S8 and S9, Supporting Information). The high-angle annular dark-field scanning transmission electron microscopy (HAADF-STEM) images and the corresponding elemental mapping images of Cr-TBA show that Cr and Br elements are uniformly distributed throughout the whole paper-clip-like structure (Figure 1d). In addition, the

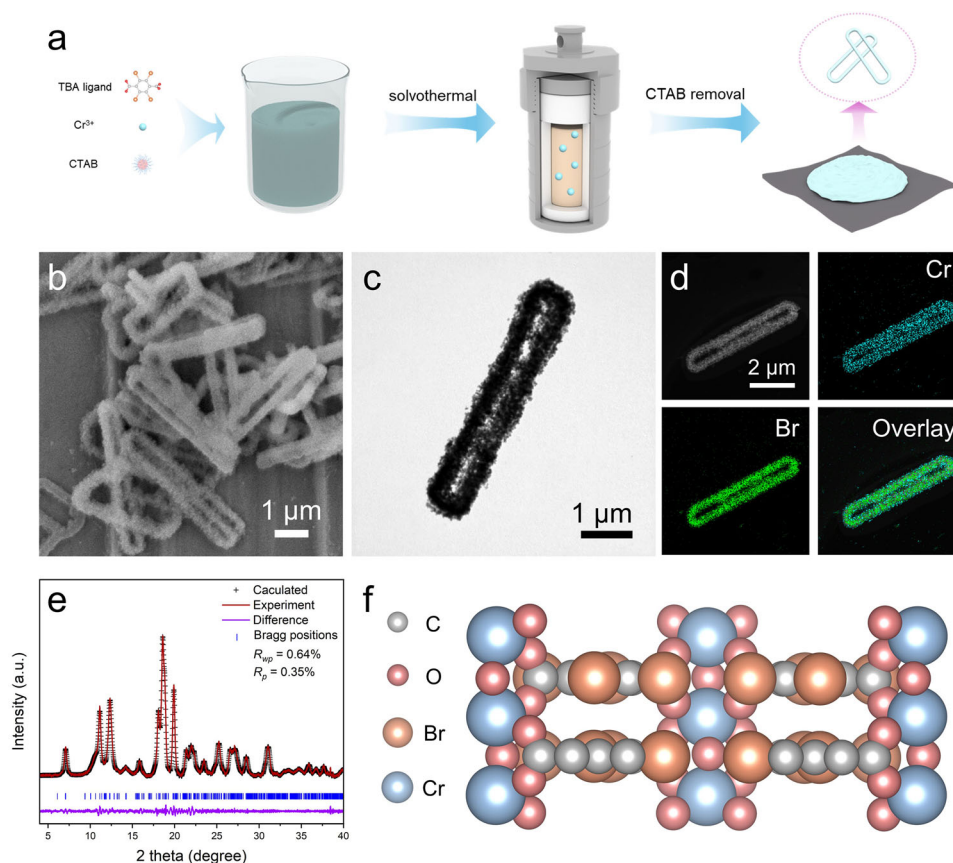


**Figure 1.** a) Schematics of the synthesis of Cr-TBA. b) FESEM, c) TEM, d) HAADF-STEM, and corresponding elemental mapping images of Cr-TBA. e) Pawley refinement of the powder XRD pattern for Cr-TBA. f) The simulated structure of the XRD pattern (with lattice parameters of  $a = 18.09$  Å,  $b = 6.82$  Å, and  $c = 10.42$  Å).

energy-dispersive X-ray spectrum verifies that Cr and Br elements co-exist in Cr-TBA sample, with the Cr species accounting for  $\approx 8.0$  wt.% (Figure S10, Supporting Information). To evaluate the specific surface area and pore size distribution of Cr-TBA prepared at different CTAB concentrations,  $N_2$  adsorption-desorption isotherms and Barrett-Joyner-Halenda pore size distribution analyses are conducted (Figure S11, Supporting Information). The specific surface areas of Cr-TBA-0, Cr-TBA-1.5, Cr-TBA, and Cr-TBA-3.5 are calculated using the Brunauer-Emmett-Teller method. Notably, the specific surface area of Cr-TBA is higher than that of other reference samples, and all samples exhibit a typical type IV adsorption isotherm with an H3-type hysteresis loop, indicating the presence of similar mesoporous structures. Fourier-transform infrared spectroscopy is employed to analyze the vibrational modes of characteristic functional groups, providing insights into the structural features of the samples. For the free ligand TBA, peaks at  $1734$  and  $1643$   $\text{cm}^{-1}$  are assigned to the asymmetric ( $\nu_{\text{as}}$ ) and symmetric ( $\nu_{\text{s}}$ ) stretching modes of the carboxylate group ( $\text{COO}^-$ ). Upon coordination with Cr ions, these peaks shift to  $1560$  and  $1427$   $\text{cm}^{-1}$ , respectively (Figure S12, Supporting Information).<sup>[26]</sup> Pawley refinement is carried out on the high-quality powder X-ray diffraction (XRD) pattern of Cr-TBA. The strong agreement between the experimental data and the calculated results further supports the simulated structure (Figure 1e,f).

The chemical state and coordination environment of the samples are investigated by X-ray photoelectron spectroscopy (XPS) and X-ray absorption fine spectroscopy (XAFS) analyses. The XPS survey spectrum of Cr-TBA exhibits the co-existence of Cr and Br species compared to that of MIL-101 (Cr) (Figure S13a, Supporting Information). In addition, the high-resolution Cr 2p XPS spectra show a slight positive shift in the binding energy of Cr 2p for Cr-TBA compared to MIL-101- $\text{NO}_2$  (Cr) and MIL-101 (Cr). This subtle variation suggests a higher oxidation state of the Cr species in Cr-TBA (Figure 2a). Meanwhile, as shown in the Br 3d spectrum of Cr-TBA, only C-Br bonding could be observed without the detection of Br ions, demonstrating the main coordination formation of Br species (Figure S13b, Supporting Information).<sup>[27]</sup>

X-ray absorption near-edge structure (XANES) and extended X-ray absorption fine structure (EXAFS) measurements are conducted to probe the local coordination environment of Cr-TBA. Figure 2b shows the Cr K-edge XANES spectra of Cr-TBA and its reference materials. The absorption threshold of Cr-TBA shows a positive shift compared to that of MIL-101 (Cr), which is in agreement with the XPS results. In addition, both exhibit an obvious positive shift compared to Cr foil, indicating the oxidized nature of Cr species.<sup>[28,29]</sup> As shown in Figure 2c, the Cr K-edge  $k^2 \chi(k)$  oscillation curve of Cr-TBA displays a similar oscillation frequency and shape to that of MIL-101 (Cr) within the range of

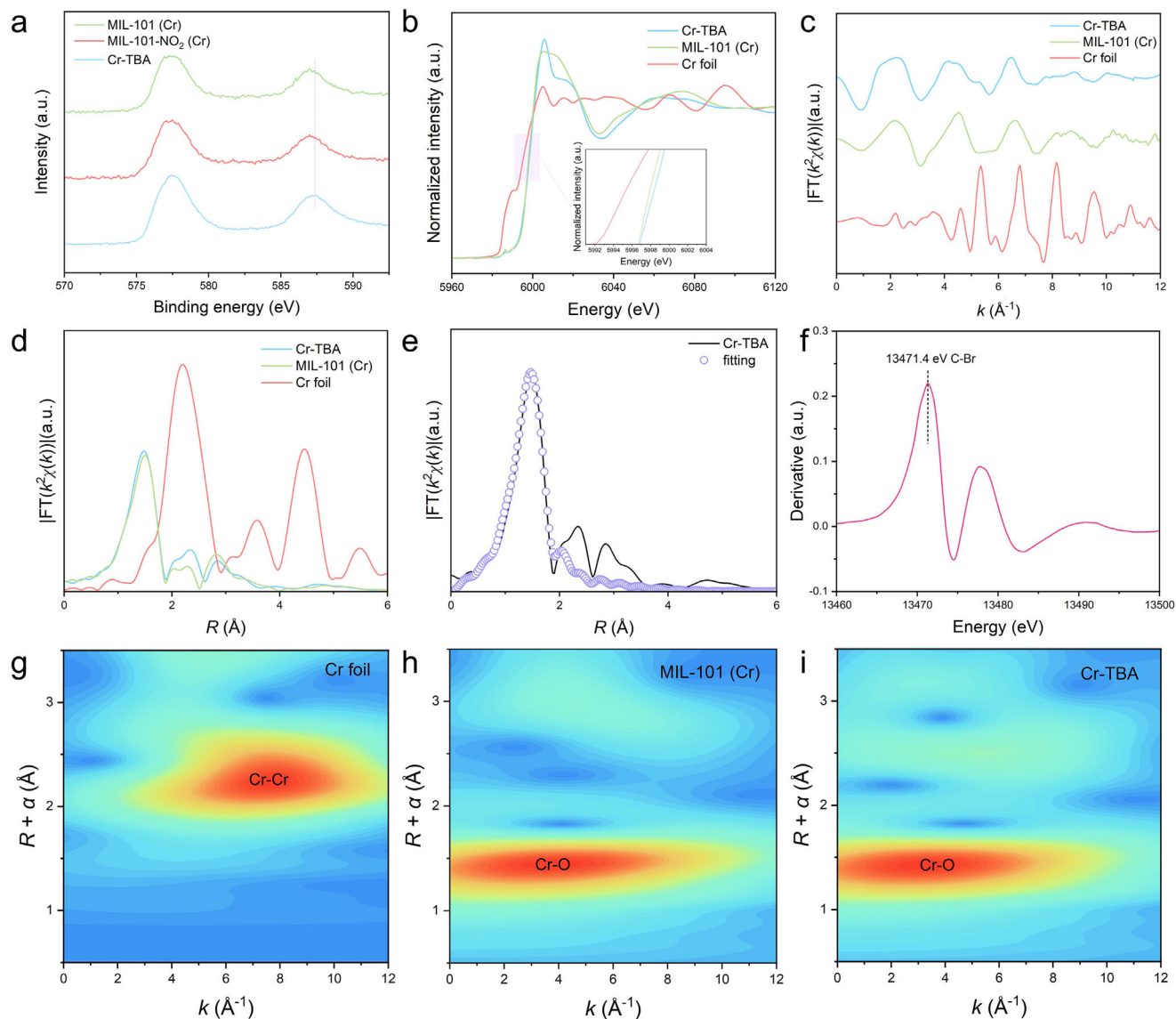


**Figure 2.** a) High-resolution Cr 2p XPS spectra of MIL-101 (Cr), MIL-101-NO<sub>2</sub> (Cr), and Cr-TBA. b) Cr K-edge XANES spectra of Cr-TBA, MIL-101 (Cr) and Cr foil. c) The  $k^2\chi(k)$  oscillation curves of Cr-TBA, MIL-101 (Cr), and Cr foil. d) FT EXAFS spectra of Cr K-edge for Cr-TBA, MIL-101 (Cr), and Cr foil. e) FT EXAFS  $R$ -space fitting results of Cr K-edge for Cr-TBA. f) XANES data of Br K-edge for Cr-TBA. WT EXAFS contour plots of Cr K-edge for g) Cr foil, h) MIL-101 (Cr), and i) Cr-TBA.

0 to 12.0 Å<sup>-1</sup>. In contrast, it differs substantially from the curve of Cr foil. This observation indicates that Cr-TBA shares a partially similar structural configuration with MIL-101 (Cr). The  $k^2$ -weighted Fourier transform (FT) EXAFS of Cr K-edge for Cr-TBA shows a dominant Cr-O coordination at 1.48 Å, which is almost identical with the Cr-O peak of MIL-101 (Cr) and corroborated by the quantitative EXAFS curve fitting analysis of Cr K-edge for Cr-TBA with the coordination number of  $\approx 6$  (Figure 2d,e; Figure S14 and Table S1, Supporting Information). Besides, there is no Cr–Cr coordination to be detected in Cr-TBA as compared to the curves of Cr foil, suggesting the formation of MOF structures (Figure 2d,e). Furthermore, the first derivative of the Br K-edge XANES data for Cr-TBA indicates the presence of C-Br coordi-

nation as the only form observed, consistent with the Br 3d XPS spectrum. This observation could be attributed to the introduction of the TBA ligand (Figure 2f). Additionally, wavelet transform (WT) EXAFS analysis is conducted to effectively differentiate and identify the backscattering atoms in the local atomic structure (Figure 2g–i). Compared to the WT contour plots of Cr foil, which display a Cr–Cr scattering path at  $\approx 8.0$  Å<sup>-1</sup>, a dominant peak corresponding to Cr-O scattering ( $\approx 4.0$  Å<sup>-1</sup>) is observed in both Cr-TBA and MIL-101(Cr), further confirming the formation of the designed MOF structure.<sup>[30–32]</sup>

To evaluate the electrocatalytic performances of Cr-TBA and related reference materials in neutral media, electrochemical 2e<sup>-</sup> ORR tests are performed in K<sub>2</sub>SO<sub>4</sub> electrolyte and calibrated to



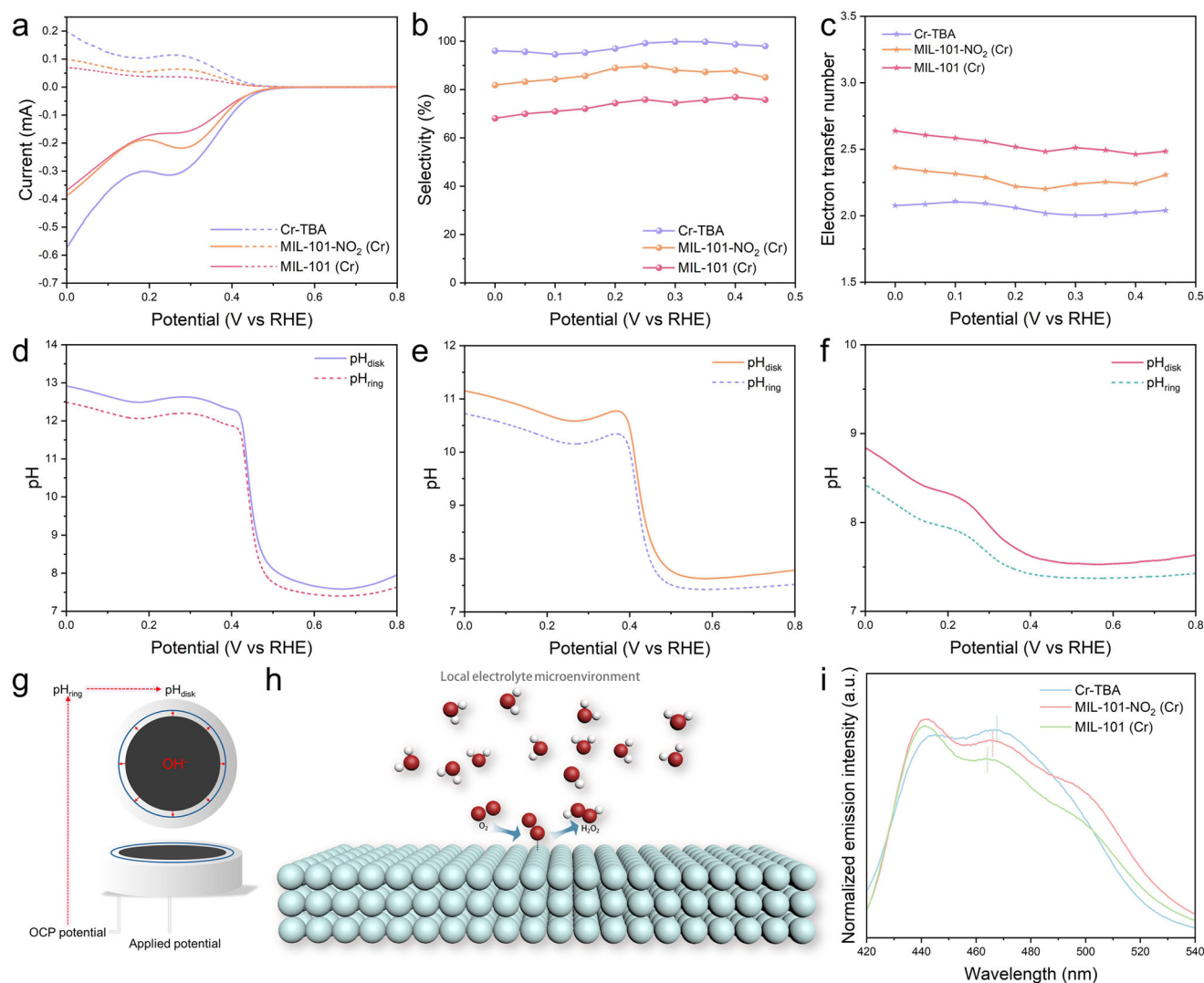


**Figure 3.** a) LSV measurements (the solid line is the disk electrode current, and the dotted line is the ring electrode current), b) calculated selectivity, and c) calculated electron transfer number of different catalysts tested with RRDE in 0.1 M  $\text{K}_2\text{SO}_4$  electrolyte. Measurements of pH on d) Cr-TBA, e) MIL-101- $\text{NO}_2$  (Cr), and f) MIL-101 (Cr) catalysts surface at different potentials in 0.1 M  $\text{K}_2\text{SO}_4$ . g) Schematic diagram for monitoring pH on the disk surface ( $\text{pH}_{\text{disk}}$ ) using an  $\text{IrO}_x$ -modified RRDE. h) Schematic diagram of Lewis acid materials adsorbing  $\text{OH}^-$  for electrosynthesis of  $\text{H}_2\text{O}_2$ . i) Fluorescence spectra of NMA binding to different samples in acetonitrile.

the reversible hydrogen electrode (RHE). In the  $\text{O}_2$ -saturated electrolyte, the linear sweep voltammetry (LSV) curves of different catalysts are tested via the rotating ring-disk electrodes (RRDE) to evaluate their  $\text{H}_2\text{O}_2$  production ability. Within the RRDE setup, the ORR occurs at the disk electrode, while the generated  $\text{H}_2\text{O}_2$  is subsequently oxidized at the ring electrode. This configuration enables the calculation of both  $\text{H}_2\text{O}_2$  selectivity and electron transfer number by correlating the currents measured at the disk and ring electrodes. As shown in LSV curves (Figure 3a), Cr-TBA not only exhibits the highest onset potential ( $E_{\text{onset}}$ ) of  $\approx 0.52$  V versus RHE, surpassing that of MIL-101 (Cr) and MIL-101- $\text{NO}_2$  (Cr) but also shows the largest current at the same applied potential. Notably, all three samples exhibit a plateau-like current at low potential regions in the  $\text{O}_2$ -saturated electrolyte. This phenomenon can be attributed to the adsorp-

tion of intermediates such as  $\text{O}_2^*$ ,  $\text{OOH}^*$ , or others at the surface of the catalysts, with delayed diffusion during the polarization curves.<sup>[33,34]</sup> In addition, the smallest Tafel slope of Cr-TBA derived from the LSV curves demonstrates its most favorable  $2e^-$  ORR kinetics (Figure S15, Supporting Information). As shown in Figure 3b,c, Cr-TBA demonstrates superior  $\text{H}_2\text{O}_2$  selectivity (over 98%) and a low electron transfer number (close to 2) in a wide potential range (0–0.45 V vs RHE), highlighting its dominant  $2e^-$  ORR ability for the  $\text{H}_2\text{O}_2$  electrosynthesis. Furthermore, to confirm the contributions of active sites, control experiments are carried out using ligand-only materials (including terephthalic acid, 2-nitroterephthalic acid, and tetrabromoterephthalic) (Figure S16, Supporting Information). These ligand-based materials exhibit a lower current density, much-reduced selectivity ( $\approx 45\%$ ), and elevated electron transfer number (over 3) in the

whole applied potential range. This comparative analysis unambiguously identifies Cr centers as the primary active sites governing the  $2e^-$  ORR performance among these three samples (Cr-TBA, MIL-101- $\text{NO}_2$  (Cr) and MIL-101 (Cr)).

To explore the possible effect of defects (missing-metal ion cluster defects and missing-linker defects) on the performance of the catalyst, the Cr-TBA catalysts synthesized with varying CTAB concentrations are evaluated. XRD patterns confirm the absence of missing-metal ion cluster defects under the current synthesis conditions, as evidenced by no discernible peaks in the  $2\theta$  range from  $4^\circ$  to  $7^\circ$  (Figure S6, Supporting Information).<sup>[35–37]</sup> Subsequently, both thermogravimetric analysis<sup>[38]</sup> and inductively coupled plasma mass spectrometry results<sup>[39]</sup> demonstrate the increased missing-linker defects in CTAB-induced samples ( $2.5 \text{ mg mL}^{-1}$ ) compared to the CTAB free samples (Figures S17 and S18, Supporting Information). Based on the above defect analysis, electrochemical performance tests are carried out to assess the impact of the defects on the catalytic behavior. As illustrated in Figure S19 (Supporting Information), CTAB-induced missing linker defects exhibit negligible deviations in  $\text{H}_2\text{O}_2$  selectivity and electron transfer number compared to the Cr-TBA performances shown in Figure 3a–c. These results demonstrate that the defect effect induced by the CTAB addition is not the primary driver of the enhanced catalytic activity in Cr-TBA.

The  $\text{IrO}_x$ -modified RRDE technique is used to quantitatively detect the pH values on the Cr-TBA, MIL-101- $\text{NO}_2$  (Cr), and MIL-101 (Cr) cathode surfaces at different applied potentials in  $0.1 \text{ M K}_2\text{SO}_4$ .<sup>[40,41]</sup> On the basis of this in situ detecting approach, a notable elevation in the pH of these catalysts could be observed during the reaction (Figure 3d–f; Figure S20, Supporting Information). Notable, Cr-TBA shows the largest pH value almost approaching 13 at an applied potential of 0 V versus RHE, far surpassing the reference catalysts, highlighting the feasibility in regulating local pH to achieve an alkaline microenvironment. This constructed local alkaline microenvironment could be attributed to the accumulation of the generated  $\text{OH}^-$  on the surface of Cr-TBA by the slow diffusion kinetics during the electrosynthesis process of  $\text{H}_2\text{O}_2$  (Figure 3g,h). NMA fluorescence is used to probe the Lewis acidity of different MOFs.<sup>[42]</sup> The fluorescence spectra of NMA coordinated to Cr-TBA, MIL-101- $\text{NO}_2$  (Cr), and MIL-101 (Cr) are shown in Figure 3i. In the case of MIL-101 (Cr) and MIL-101- $\text{NO}_2$  (Cr), the fluorescence maxima ( $\lambda_{\text{max}}$ ) of NMA change dramatically from 437.5 to 464.1 and 465.9 nm, respectively (Figure 3i; Figure S21, Supporting Information). By contrast, Cr-TBA causes the largest shift, with a  $\lambda_{\text{max}}$  of 467.7 nm. Quantitative Lewis acidity test results prove that the introduction of TBA ligand to Cr sites increases the Lewis acidity of Cr-TBA obviously, which is beneficial to its adsorption of  $\text{OH}^-$ , thereby improving its performance of electrosynthesis of  $\text{H}_2\text{O}_2$ .

Furthermore, pH values on the electrode surface of Cr-TBA materials prepared with different concentrations of CTAB are analyzed during the electrochemical synthesis of  $\text{H}_2\text{O}_2$ . The results show that the changes in specific surface area, pore structure and morphology caused by the addition of CTAB have no significant effect on its ability to accumulate  $\text{OH}^-$  during the electrocatalytic process (Figure S22, Supporting Information). Similarly, these structural variations exhibit no measurable impact on  $2e^-$  ORR selectivity (Figure S19, Supporting Information). Consequently, the intrinsic Lewis acidity of the catalysts, arising from

their unique structural features, is identified as the dominant factor modulating the reaction microenvironment, thereby governing  $2e^-$  ORR performances in neutral electrolytes.

To further evaluate the  $2e^-$  ORR performance, the  $\text{H}_2\text{O}_2$  production capacities of these samples are determined using flow-cell reactors with gas-diffusion electrodes (Figure 4a; Figure S23, Supporting Information) by using a titration method based on the reaction of  $\text{H}_2\text{O}_2$  with  $\text{Ce}^{4+}$  (Figure S24, Supporting Information).<sup>[43]</sup> As expected, Cr-TBA exhibits the highest Faradaic efficiency for the production of  $\text{H}_2\text{O}_2$  at the current density of  $50 \text{ mA cm}^{-2}$  ( $\approx 98\%$ ) (Figure 4b). Meanwhile, it could also achieve a remarkable  $\text{H}_2\text{O}_2$  production rate with  $\approx 4.5 \text{ mol g}_{\text{cat}}^{-1} \text{ h}^{-1}$  in  $0.1 \text{ M K}_2\text{SO}_4$  (Figure 4c). Notably, the cumulative  $\text{H}_2\text{O}_2$  yield of Cr-TBA increases linearly within a 1 h continuous test, indicating stable and highly efficient  $\text{H}_2\text{O}_2$  production. Furthermore, LSV curves of Cr-TBA and MIL-101 (Cr) are recorded in neutral electrolytes as well, showing the reduced overpotential and improved  $2e^-$  ORR activity of Cr-TBA in flow-cell reactors (Figure 4d). To further assess the electrochemical synthesis of  $\text{H}_2\text{O}_2$  performances of Cr-TBA, LSV curves are measured in  $0.25 \text{ M}$  and  $0.5 \text{ M K}_2\text{SO}_4$  (Figure S25, Supporting Information). The results indicate that Cr-TBA exhibits a consistent  $E_{\text{onsite}}$  across different concentrations of  $\text{K}_2\text{SO}_4$  electrolytes. Notably, in  $0.5 \text{ M K}_2\text{SO}_4$ , it could achieve a remarkably higher current density at the same potential compared to the other concentration. Meanwhile, the Cr-TBA catalyst demonstrates a Faradaic efficiency exceeding 96% in both  $0.25 \text{ M}$  and  $0.5 \text{ M K}_2\text{SO}_4$  (Figures S26 and S27, Supporting Information). Additionally, its  $\text{H}_2\text{O}_2$  production rates could reach 9.1 and  $13.4 \text{ mol g}_{\text{cat}}^{-1} \text{ h}^{-1}$  in these concentrations, respectively (Figures S26 and S27, Supporting Information). Noteworthy, at a higher industrial-scale current density of  $250 \text{ mA cm}^{-2}$ , the Cr-TBA catalyst can still achieve a high Faradic efficiency of over 85% (Figure S28, Supporting Information). These impressive yields and efficiencies surpass most recently reported catalysts for  $\text{H}_2\text{O}_2$  electrosynthesis in neutral electrolytes, underscoring its potential for industrial application (Figure 4e; Tables S2 and S3, Supporting Information).<sup>[16,18,19,44–50]</sup> Besides, by utilization of the device in Figure 4a, Cr-TBA demonstrates the negligible variation of activity, Faradaic efficiency, and morphology after the stability test (Figure 4h; Figures S29 and S30, Supporting Information). The above excellent stability could originate from the stable structural features of Cr-TBA after the reactions. These findings underscore the exceptional potential of Cr-TBA for its electrochemical synthesis of  $\text{H}_2\text{O}_2$  application in neutral electrolytes.

To elucidate the mechanisms underlying the substantially enhanced  $2e^-$  ORR performance after manipulating the local microenvironment of Cr-TBA, operando attenuated total reflection surface-enhanced infrared absorption spectroscopy (ATR-SEIRAS) is performed (Figure S31, Supporting Information). As shown in Figure 5a,b, a main band at  $\approx 1100 \text{ cm}^{-1}$  could be attributed to the O stretching vibration of surface-adsorbed  $^*\text{OOH}$ .<sup>[51]</sup> During the application of negative potential, the band intensity of  $^*\text{OOH}$  continues to increase for both Cr-TBA and MIL-101 (Cr). However, compared to MIL-101 (Cr), Cr-TBA exhibits an identifiable  $^*\text{HOOH}$  band at  $\approx 1370 \text{ cm}^{-1}$ , as well as the obvious  $^*\text{OOH}$  band with weaker intensity, demonstrating its lower intermediate adsorption strength on Cr site with the favorable formation process of  $\text{H}_2\text{O}_2$ . The different frequencies

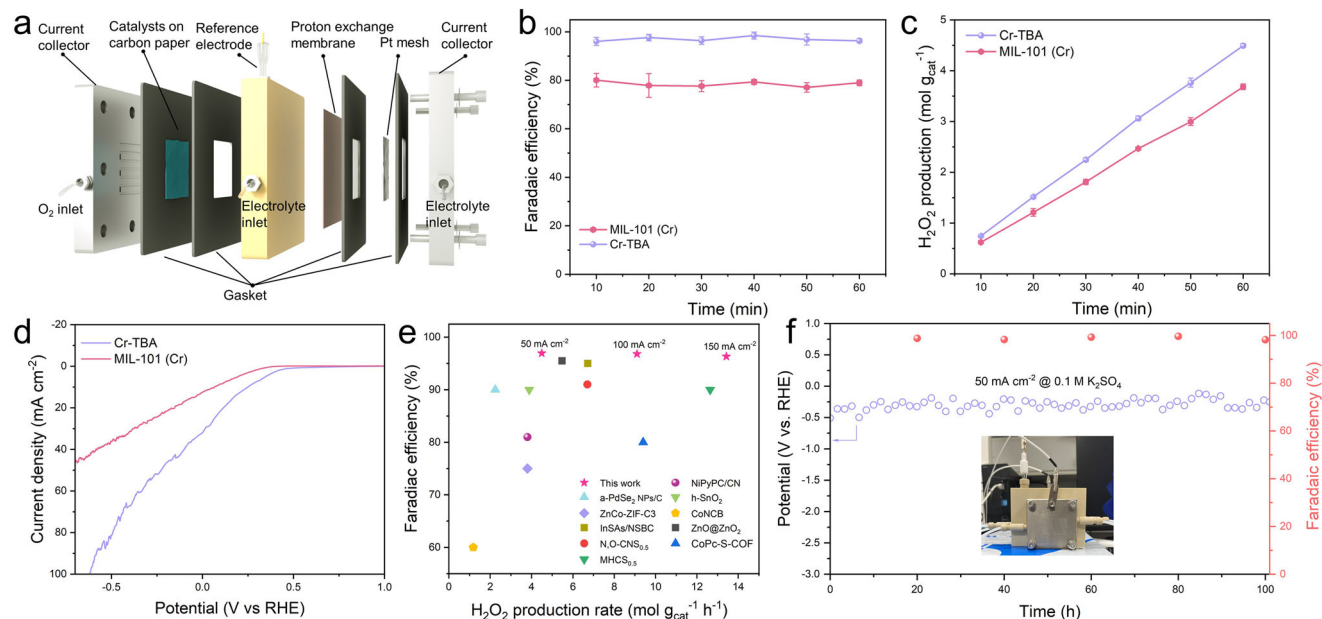


**Figure 4.** a) Schematics of the flow cell for electrocatalytic  $\text{O}_2$  reduction to  $\text{H}_2\text{O}_2$ . b) Faradaic efficiency, c)  $\text{H}_2\text{O}_2$  production amount, and d) LSV curves of Cr-TBA and MIL-101 (Cr) in  $0.1 \text{ M K}_2\text{SO}_4$ . e) Performance comparison of this work with some recently reported electrocatalysts for electrosynthesis of  $\text{H}_2\text{O}_2$  in neutral media. f) Stability test of Cr-TBA at  $50 \text{ mA cm}^{-2}$  in  $0.1 \text{ M K}_2\text{SO}_4$  (inset is the photograph of the flow cell).

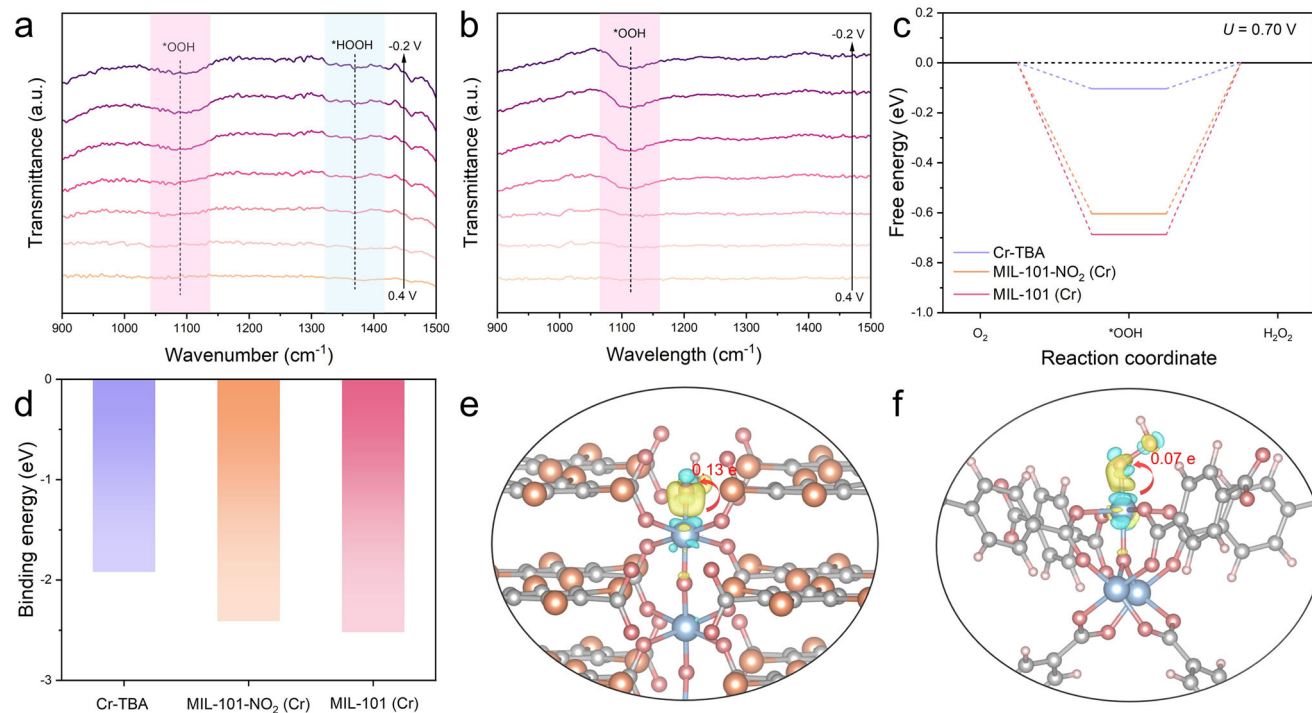


**Figure 5.** Operando ATR-SEIRAS collected on a) Cr-TBA and b) MIL-101 (Cr) in  $\text{O}_2$ -saturated  $0.1 \text{ M K}_2\text{SO}_4$  solution. c) Free energy diagram at  $U = 0.70 \text{ V}$  of Cr-TBA, MIL-101- $\text{NO}_2$  (Cr), and MIL-101 (Cr). d) Binding energies of  $^*\text{OOH}$  intermediate on Cr-TBA, MIL-101- $\text{NO}_2$  (Cr), and MIL-101 (Cr). Charge density difference of e) Cr-TBA and f) MIL-101 (Cr), and the corresponding charge accumulation in the  $^*\text{OOH}$  intermediate (The white, pink spheres represent H atoms, the light red spheres represent O atoms, the light blue spheres represent Cr atoms, and the light orange spheres represent Br atoms. The yellow and cyan contours represent charge accumulation and depletion in the real space with an isosurface level of  $\pm 0.0015 \text{ |e| Bohr}^3$ , respectively).

of  $^*\text{OOH}$  band ( $\nu_{\text{O-O}}$ ) between Cr-TBA and MIL-101 (Cr) catalysts should be attributed to the pH effect during the reaction process, which is consistent with the observations in the literature.<sup>[41]</sup>

DFT calculations are subsequently performed to understand the catalytic mechanism of Cr-TBA. The greater propensity of Cr-TBA for the  $2\text{e}^-$  ORR process is confirmed by the climbing-image nudged elastic band method, which shows a lower energy barrier for the  $2\text{e}^-$  pathway (0.29 eV) compared to the  $4\text{e}^-$  pathway (1.29 eV) (Figure S32, Supporting Information). In addition, as shown in the free energy diagram at zero electrode potential ( $U = 0$  V), all elementary steps of ORR are exothermic, showing these elementary steps are thermodynamically favorable (Figure S33, Supporting Information). Free energy diagrams of different models at the equilibrium potential ( $U = 0.7$  V) of  $2\text{e}^-$  ORR are calculated. For the Cr-TBA model, the Cr site exhibits the lowest energy barrier both before and after considering the implicit solvation effect (Figure 5c; Figure S34, Supporting Information), which is consistent with the electrochemical results. Additionally, when considering the pH effect, the thermodynamic limit potential of  $\text{H}_2\text{O}_2$  is changed from 0.70 to 0.76 V versus RHE ( $\text{pH} > 11.6$ ),<sup>[52]</sup> resulting in the smaller energy barrier of Cr-TBA for electrosynthesis of  $\text{H}_2\text{O}_2$  (Figure S35, Supporting Information). These results verify the favorable microenvironment regulation strategy in designing Cr-TBA for electrochemical synthesis of  $\text{H}_2\text{O}_2$  in neutral electrolytes. In addition, the binding energy of the  $^*\text{OOH}$  intermediate on Cr-TBA, as observed by operando ATR-SEIRAS, aligns with the weakest binding energy obtained in DFT calculations (Figure 5d). Despite the relatively weak binding energy of Cr-TBA, its free energy level is in closer proximity to the ideal value, rendering it more favorable for the formation of  $\text{H}_2\text{O}_2$  (Figure 5c). In addition, the analysis of the charge density difference suggests a more prominent electron transfer from the Cr sites in Cr-TBA to the adsorbed  $^*\text{OOH}$  intermediates ( $0.13\text{e}^-$ ), compared to the results with MIL-101 (Cr) ( $0.07\text{e}^-$ ) (Figure 5e,f). This indicates that Cr-TBA could be more beneficial for the electron accumulation around the adsorbed  $^*\text{OOH}$ , thus facilitating the reduction of  $\text{O}_2$  to  $\text{H}_2\text{O}_2$ . The above DFT calculation results show the substantial impact of the introduction of TBA ligand for high efficiency and high selectivity  $\text{H}_2\text{O}_2$  electrosynthesis.

### 3. Conclusion

In summary, a MOF of Cr metal sites coordinated with tetrabromoterephthalic acid ligand (Cr-TBA) is synthesized via an elaborately designed crystal nucleation and growth process successfully. The Lewis acidity of Cr-TBA could be increased obviously compared to the pristine MIL-101 (Cr), resulting in the local pH elevation during the electrosynthesis of the  $\text{H}_2\text{O}_2$  process. The modified local microenvironment could be beneficial for the transformation from  $\text{OOH}^*$  intermediates to  $\text{H}_2\text{O}_2$ , thus substantially facilitating the electrosynthesis  $\text{H}_2\text{O}_2$  performances in the neutral electrolyte, achieving the remarkable Faradaic efficiency of 96–98% at the current density of 50 to 150  $\text{mA cm}^{-2}$  with the maximum  $\text{H}_2\text{O}_2$  production rate of 13.4  $\text{mol g}_{\text{cat}}^{-1} \text{h}^{-1}$ . This work offers new insights into enhancing the electrocatalytic performance of catalysts by regulating the local reaction microenvironment, thus facilitating their practical applications in the field of energy storage and conversion. In addition, further exploration is still needed to develop scalable production methods and ensure

consistent performance under varied operating conditions typically encountered in real industrial settings.

### Supporting Information

Supporting Information is available from the Wiley Online Library or from the author.

### Acknowledgements

X.W.L. acknowledges the funding support for the Global STEM Professorship from the Innovation, Technology and Industry Bureau ("ITIB") and Education Bureau ("EDB") of Hong Kong.

### Conflict of Interest

The authors declare no conflict of interest.

### Data Availability Statement

The data that support the findings of this study are available from the corresponding author upon reasonable request.

### Keywords

hydrogen peroxide, microenvironment regulation, paper-clip-like structures, two-electron oxygen reduction reaction

Received: January 6, 2025  
Revised: March 9, 2025  
Published online: March 30, 2025

- [1] C. Xia, Y. Xia, P. Zhu, L. Fan, H. Wang, *Science* **2019**, 366, 226.
- [2] Y. Bu, R. Ma, Y. Wang, Y. Zhao, F. Li, G.-F. Han, J.-B. Baek, *Adv. Mater.* **2024**, 36, 2412670.
- [3] Z. Pei, Y. Li, G. Fan, Y. Guo, D. Luan, X. Gu, X. W. Lou, *Small* **2024**, 20, 2403808.
- [4] Y. Li, D. Luan, X. W. Lou, *Adv. Mater.* **2024**, 36, 2412386.
- [5] X. Shi, S. Back, T. M. Gill, S. Siahrostami, X. Zheng, *Chem* **2021**, 7, 38.
- [6] Z. Pei, H. Zhang, Y. Guo, D. Luan, X. Gu, X. W. Lou, *Adv. Mater.* **2024**, 36, 2306047.
- [7] L. Jing, W. Wang, Q. Tian, Y. Kong, X. Ye, H. Yang, Q. Hu, C. He, *Angew. Chem., Int. Ed.* **2024**, 63, 202403023.
- [8] Y. Bu, Y. Wang, G.-F. Han, Y. Zhao, X. Ge, F. Li, Z. Zhang, Q. Zhong, J.-B. Baek, *Adv. Mater.* **2021**, 33, 2103266.
- [9] Y. Liu, P. Wang, L. Xie, Y. Xia, S. Zhan, W. Hu, Y. Li, *Angew. Chem., Int. Ed.* **2024**, 63, 202319470.
- [10] L.-Y. Dong, J.-S. Wang, T.-Y. Li, T. Wu, X. Hu, Y.-T. Wu, M.-Y. Zhu, G.-P. Hao, A.-H. Lu, *Angew. Chem., Int. Ed.* **2024**, 63, 202317660.
- [11] W. Peng, J. Liu, X. Liu, L. Wang, L. Yin, H. Tan, F. Hou, J. Liang, *Nat. Commun.* **2023**, 14, 4430.
- [12] Q. Chang, P. Zhang, A. H. B. Mostaghimi, X. Zhao, S. R. Denny, J. H. Lee, H. Gao, Y. Zhang, H. L. Xin, S. Siahrostami, J. G. Chen, Z. Chen, *Nat. Commun.* **2020**, 11, 2178.
- [13] C. Zhang, W. Shen, K. Guo, M. Xiong, J. Zhang, X. Lu, *J. Am. Chem. Soc.* **2023**, 145, 11589.



- [14] X. Zhang, X. Zhao, P. Zhu, Z. Adler, Z.-Y. Wu, Y. Liu, H. Wang, *Nat. Commun.* **2022**, *13*, 2880.
- [15] Y. Chen, C. Zhen, Y. Chen, H. Zhao, Y. Wang, Z. Yue, Q. Wang, J. Li, M. D. Gu, Q. Cheng, H. Yang, *Angew. Chem., Int. Ed.* **2024**, *63*, 202407163.
- [16] L. Liu, L. Kang, J. Feng, D. G. Hopkinson, C. S. Allen, Y. Tan, H. Gu, I. Mikulska, V. Celorrio, D. Gianolio, T. Wang, L. Zhang, K. Li, J. Zhang, J. Zhu, G. Held, P. Ferrer, D. Grinter, J. Callison, M. Wilding, S. Chen, I. Parkin, G. He, *Nat. Commun.* **2024**, *15*, 4079.
- [17] C. Santoro, P. Bollella, B. Erable, P. Atanassov, D. Pant, *Nat. Catal.* **2022**, *5*, 473.
- [18] Y. Zhang, M. Wang, W. Zhu, M. Fang, M. Ma, F. Liao, H. Yang, T. Cheng, C.-W. Pao, Y.-C. Chang, Z. Hu, Q. Shao, M. Shao, Z. Kang, *Angew. Chem., Int. Ed.* **2023**, *62*, 202218924.
- [19] L. Jing, Q. Tian, W. Wang, X. Li, Q. Hu, H. Yang, C. He, *Adv. Energy Mater.* **2024**, *14*, 2304418.
- [20] Z. Shen, G. Chen, X. Cheng, F. Xu, H. Huang, X. Wang, L. Yang, Q. Wu, Z. Hu, *Sci. Adv.* **2024**, *10*, adm9325.
- [21] H. Hu, Z. Zhang, L. Liu, X. Che, J. Wang, Y. Zhu, J. P. Attfield, M. Yang, *Sci. Adv.* **2024**, *10*, adn7012.
- [22] Y. Hu, Z. Fang, X. Wan, X. Ma, Y. Wang, M. Dong, Z. Ye, X. Peng, *ACS Sustainable Chem. Eng.* **2022**, *10*, 6446.
- [23] T.-L. Ho, *Chem. Rev.* **1975**, *75*, 1.
- [24] Y. Yuan, W. Wang, L. Qiu, F. Peng, X. Jiang, A. Xie, Y. Shen, X. Tian, L. Zhang, *Mater. Chem. Phys.* **2011**, *131*, 358.
- [25] R. L. Whetten, W. M. Gelbart, *J. Phys. Chem.* **1994**, *98*, 3544.
- [26] Y.-F. Wang, H.-Y. An, Q. Mao, L.-T. He, S.-Y. Li, J.-M. Li, *J. Cluster Sci.* **2024**, *35*, 2591.
- [27] S. Ji, B. Jiang, H. Hao, Y. Chen, J. Dong, Y. Mao, Z. Zhang, R. Gao, W. Chen, R. Zhang, Q. Liang, H. Li, S. Liu, Y. Wang, Q. Zhang, L. Gu, D. Duan, M. Liang, D. Wang, X. Yan, Y. Li, *Nat. Catal.* **2021**, *4*, 407.
- [28] Y. He, X. Yang, Y. Li, L. Liu, S. Guo, C. Shu, F. Liu, Y. Liu, Q. Tan, G. Wu, *ACS Catal.* **2022**, *12*, 1216.
- [29] Z. Pei, H. Zhang, Z.-P. Wu, X. F. Lu, D. Luan, X. W. Lou, *Sci. Adv.* **2023**, *9*, adh1320.
- [30] Z.-Y. Wu, M. Karamad, X. Yong, Q. Huang, D. A. Cullen, P. Zhu, C. Xia, Q. Xiao, M. Shakouri, F.-Y. Chen, J. Y. Kim, Y. Xia, K. Heck, Y. Hu, M. S. Wong, Q. Li, I. Gates, S. Siahrostami, H. Wang, *Nat. Commun.* **2021**, *12*, 2870.
- [31] X. Zhao, R. Fang, F. Wang, X. Kong, Y. Li, *JACS Au* **2023**, *3*, 185.
- [32] Z. Yang, Y. Wang, M. Zhu, Z. Li, W. Chen, W. Wei, T. Yuan, Y. Qu, Q. Xu, C. Zhao, X. Wang, P. Li, Y. Li, Y. Wu, Y. Li, *ACS Catal.* **2019**, *9*, 2158.
- [33] H. Chen, C. He, H. Niu, C. Xia, F.-M. Li, W. Zhao, F. Song, T. Yao, Y. Chen, Y. Su, W. Guo, B. Y. Xia, *J. Am. Chem. Soc.* **2024**, *146*, 15356.
- [34] K. Jiang, S. Back, A. J. Akey, C. Xia, Y. Hu, W. Liang, D. Schaak, E. Stavitski, J. K. Nørskov, S. Siahrostami, H. Wang, *Nat. Commun.* **2019**, *10*, 3997.
- [35] G. C. Shearer, S. Chavan, S. Bordiga, S. Svelle, U. Olsbye, K. P. Lillerud, *Chem. Mater.* **2016**, *28*, 3749.
- [36] D. K. Sannes, S. Øien-Ødegaard, E. Aunan, A. Nova, U. Olsbye, *Chem. Mater.* **2023**, *35*, 3793.
- [37] L. Liu, Z. Chen, J. Wang, D. Zhang, Y. Zhu, S. Ling, K.-W. Huang, Y. Belmabkhout, K. Adil, Y. Zhang, B. Slater, M. Eddaoudi, Y. Han, *Nat. Chem.* **2019**, *11*, 622.
- [38] J. Ren, M. Ledwaba, N. M. Musyoka, H. W. Langmi, M. Mathe, S. Liao, W. Pang, *Coord. Chem. Rev.* **2017**, *349*, 169.
- [39] Y. Liang, Z. Zhang, X. Su, X. Feng, S. Xing, W. Liu, R. Huang, Y. Liu, *Angew. Chem., Int. Ed.* **2023**, *62*, 202309030.
- [40] Y. Yokoyama, K. Miyazaki, Y. Kondo, Y. Miyahara, T. Fukutsuka, T. Abe, *Chem. Lett.* **2020**, *49*, 195.
- [41] J. Guo, Y. Zheng, Z. Hu, C. Zheng, J. Mao, K. Du, M. Jaroniec, S.-Z. Qiao, T. Ling, *Nat. Energy* **2023**, *8*, 1418.
- [42] P. Ji, T. Drake, A. Murakami, P. Oliveres, J. H. Skone, W. Lin, *J. Am. Chem. Soc.* **2018**, *140*, 10553.
- [43] J. Gao, H. b. Yang, X. Huang, S.-F. Hung, W. Cai, C. Jia, S. Miao, H. M. Chen, X. Yang, Y. Huang, T. Zhang, B. Liu, *Chem* **2020**, *6*, 658.
- [44] L. Sun, X. Jin, T. Su, A. C. Fisher, X. Wang, *Adv. Mater.* **2024**, *36*, 2306336.
- [45] Z. Yu, S. Lv, Q. Yao, N. Fang, Y. Xu, Q. Shao, C.-W. Pao, J.-F. Lee, G. Li, L.-M. Yang, X. Huang, *Adv. Mater.* **2023**, *35*, 2208101.
- [46] C. Zhang, L. Yuan, C. Liu, Z. Li, Y. Zou, X. Zhang, Y. Zhang, Z. Zhang, G. Wei, C. Yu, *J. Am. Chem. Soc.* **2023**, *145*, 7791.
- [47] E. Zhang, L. Tao, J. An, J. Zhang, L. Meng, X. Zheng, Y. Wang, N. Li, S. Du, J. Zhang, D. Wang, Y. Li, *Angew. Chem., Int. Ed.* **2022**, *61*, 202117347.
- [48] Y. Zhou, L. Xu, J. Wu, W. Zhu, T. He, H. Yang, H. Huang, T. Cheng, Y. Liu, Z. Kang, *Energy Environ. Sci.* **2023**, *16*, 3526.
- [49] Q. Zhi, R. Jiang, X. Yang, Y. Jin, D. Qi, K. Wang, Y. Liu, J. Jiang, *Nat. Commun.* **2024**, *15*, 678.
- [50] Q. Tian, L. Jing, H. Du, Y. Yin, X. Cheng, J. Xu, J. Chen, Z. Liu, J. Wan, J. Liu, J. Yang, *Nat. Commun.* **2024**, *15*, 983.
- [51] Y. Sun, K. Fan, J. Li, L. Wang, Y. Yang, Z. Li, M. Shao, X. Duan, *Nat. Commun.* **2024**, *15*, 6098.
- [52] P. Cao, X. Quan, X. Nie, K. Zhao, Y. Liu, S. Chen, H. Yu, J. G. Chen, *Nat. Commun.* **2023**, *14*, 172.